

OPEN ACCESS

First tests of a novel radiation hard CMOS sensor process for Depleted Monolithic Active Pixel Sensors

To cite this article: H. Pernegger *et al* 2017 *JINST* **12** P06008

View the [article online](#) for updates and enhancements.

You may also like

- [A review of advances in pixel detectors for experiments with high rate and radiation](#)
Maurice Garcia-Sciveres and Norbert Wermes
- [A high frame rate, 16 million pixels, radiation hard CMOS sensor](#)
N Guerrini, R Turchetta, G Van Hoften et al.
- [Development of a Depleted Monolithic CMOS Sensor in a 150 nm CMOS Technology for the ATLAS Inner Tracker Upgrade](#)
T. Wang, P. Rymaszewski, M. Barbero et al.



The
Electrochemical
Society

Advancing solid state &
electrochemical science & technology



DISCOVER
how sustainability
intersects with
electrochemistry & solid
state science research



First tests of a novel radiation hard CMOS sensor process for Depleted Monolithic Active Pixel Sensors

H. Pernegger,^{a,1,2} R. Bates,^c C. Buttar,^c M. Dalla,^b J.W. van Hoorne,^a T. Kugathasan,^a
D. Maneuski,^c L. Musa,^a P. Riedler,^a C. Riegel,^a C. Sbarra,^b D. Schaefer,^a E.J. Schioppa^a
and W. Snoeys^a

^aCERN Experimental Physics Department,
CH-1211 Geneva 23, Switzerland

^bUniversità e INFN,
I-40127 Bologna, Italy

^cSUPA School of Physics and Astronomy, University of Glasgow,
Glasgow, G12 8QQ, U.K.

E-mail: heinz.pernegger@cern.ch

ABSTRACT: The upgrade of the ATLAS [1] tracking detector for the High-Luminosity Large Hadron Collider (LHC) at CERN requires novel radiation hard silicon sensor technologies. Significant effort has been put into the development of monolithic CMOS sensors but it has been a challenge to combine a low capacitance of the sensing node with full depletion of the sensitive layer. Low capacitance brings low analog power. Depletion of the sensitive layer causes the signal charge to be collected by drift sufficiently fast to separate hits from consecutive bunch crossings (25 ns at the LHC) and to avoid losing the charge by trapping. This paper focuses on the characterization of charge collection properties and detection efficiency of prototype sensors originally designed in the framework of the ALICE Inner Tracking System (ITS) upgrade [2]. The prototypes are fabricated both in the standard TowerJazz³ 180nm CMOS imager process [3] and in an innovative modification of this process developed in collaboration with the foundry, aimed to fully deplete the sensitive epitaxial layer and enhance the tolerance to non-ionizing energy loss. Sensors fabricated in standard and modified process variants were characterized using radioactive sources, focused X-ray beam and test beams before and after irradiation. Contrary to sensors manufactured in the standard process, sensors from the modified process remain fully functional even after a dose of $10^{15} n_{eq}/cm^2$, which is the expected NIEL radiation fluence for the outer pixel layers in the future ATLAS Inner Tracker (ITk) [4].

KEYWORDS: Analogue electronic circuits; Particle tracking detectors (Solid-state detectors); Pixelated detectors and associated VLSI electronics; Solid state detectors

¹Corresponding author.

²Mailing address: Heinz Pernegger, CERN EP Department, CH-1211 Geneva, Switzerland.

³Manufactured by Tower Semiconductor Ltd, Israel.

Contents

| | | |
|----------|--|-----------|
| 1 | Introduction | 1 |
| 2 | The TowerJazz Investigator chip | 2 |
| 3 | Setup and analysis | 3 |
| 4 | Charge collection measurements of sensors produced in the standard and modified process | 5 |
| 4.1 | Signal response of sensors with large pixel pitch | 5 |
| 4.2 | Position resolved charge collection behaviour | 7 |
| 4.3 | Charge collection and signal rise-times in the standard and modified process | 8 |
| 5 | Irradiation results | 10 |
| 5.1 | Standard process after irradiation | 11 |
| 5.2 | Modified process after irradiation | 11 |
| 6 | Beam Test results | 13 |
| 6.1 | Measurement of cluster size | 14 |
| 6.2 | Measurement of sensor efficiency | 15 |
| 6.3 | Efficiency before irradiation | 16 |
| 6.4 | Efficiency after irradiation | 18 |
| 7 | Summary | 18 |

1 Introduction

Particle tracking in proton-proton collider experiments sets stringent demands on sensors and readout electronics. In the context of the ATLAS CMOS sensor development collaboration we investigate the use of new radiation hard CMOS sensors for the potential application as tracking detectors in the upgrade of the ATLAS experiment [1] for the High-Luminosity Large Hadron Collider at CERN. Currently ATLAS uses hybrid pixel detectors [5], which consist of a silicon sensor, usually produced on high resistivity float-zone wafers, and the readout electronics chip. Their assembly requires a fine-pitch bump bonding process for interconnection between sensor and readout chip. This impacts the possible segmentation, the material budget, and the cost. The increasing availability of commercial high-voltage and/or high-resistivity CMOS imaging technologies provide a possible alternative to hybrid pixel detectors through a Depleted Monolithic Active Pixel Sensor (DMAPS) implemented in the CMOS processes with typical feature size of 150nm to 350nm. In DMAPS the ASIC includes the sensor, which collects the ionisation charge by drift in a depleted region, and the readout circuit.

This paper is dedicated to the evaluation of the DMAPS test chip prototypes designed during the developments for the upgrade of the ALICE Inner Tracking System (ITS). The prototypes have been fabricated in the standard TowerJazz 180nm CMOS imaging process and in a modified version of this process aimed to fully deplete the sensitive epitaxial layer and enhance tolerance to non-ionizing energy loss [6]. Charge collection properties and detection efficiency of these prototypes have been studied before and after irradiation to verify whether a particular pixel design in one process variant would carry potential for the upgrade of the ATLAS ITk, where the sensors require two orders of magnitude higher radiation hardness ($\approx 10^{15} n_{eq}/cm^2$ for the outer pixel layers) and signal speed as compared to the ALICE ITS.

2 The TowerJazz Investigator chip

The “Investigator” sensor chip [6–8] has been produced in the TowerJazz 180nm CMOS imager process during the course of the development of monolithic CMOS sensors for the ALICE experiment.

The sensor chip consists of 134 pixel sub-matrices of different designs. Each sub-matrix consists of an active 8×8 pixels matrix where each pixel is connected to an input transistor and a reset transistor. Each input transistor is connected via two signal buffers to the chip periphery. The chip allows simultaneous measurement of the analog signals on 64 pixels. The output signal amplitude is proportional to the ionisation charge collected on the input transistor, the front-end and output circuit limits the rise-time of the signal to between 10ns and 15ns.

Figure 1 shows the top-view of a sub-matrix (a) and pixel (b) as well as the cross-section of a pixel in the standard process (c). The ionisation charge generated by the incident charged particle in the $25\mu m$ thick epitaxial layer is collected by the n-well. Using the deep p-well as a shield, CMOS circuits can be implemented in the pixel cell. By applying a negative voltage to the deep p-well and p-type substrate with respect to the collection electrode, a region in the epitaxial layer gets depleted as indicated in white. In this zone ionisation charge is collected by drift in the electric field. Outside this region, charge motion is dominated by diffusion, hence the induced signal will be slower and ionisation charge is more prone to trapping, i.e. by radiation induced charge traps. Chips tested for this paper have a final p^+ -substrate thickness of $65\mu m$. Table 1 summarises the TowerJazz imaging process main features used for the sensor presented here.

The charge collection electrode size and spacing parameters in table 1 are shown in figure 1b. The n-type collection electrode sits in the center of an opening in the p-well and deep p-well in the pixel center. The size of the opening is given by the diameter of the electrode plus twice the spacing between collection n-well and surrounding p-well. The extent and shape of the depleted zone depends on geometrical parameters like diameter of n-type collection well and the spacing between collection n-well and deep p-well, as well as the epitaxial layer thickness. After processing, the wafer are thinned to $100\mu m$ and diced. Table 2 summarises the pixels design choices, which are tested for this publication. Note that $25 \times 25\mu m^2$ to $30 \times 30\mu m^2$ pixels possess a small spacing ($3\mu m$) between collection n-well and deep p-well while the $50 \times 50\mu m^2$ matrix have a large spacing ($18.5\mu m$). These differences in pitch and spacing play a significant role in the signal response as they influence the detector capacitance and signal amplification as will be shown in later sections.

The depletion zone and charge collection is further influenced by the epitaxial layer resistivity and applied substrate voltage. The optimal choice will minimise the capacitance, maximize the

Table 1. Overview of the technology options for the TowerJazz process.

| Feature | Property |
|----------------------|--|
| MOS channel length | 180nm |
| Metals | 6 layers, Aluminum |
| Supply rail | 1.8V (up to -6V on substrate) |
| MOS transistor types | full CMOS |
| Wafer type | epi p-type $25\mu\text{m}$ ($>1\text{k}\Omega\text{cm}$) thickness on p-type substrate |
| Backside implant | none |

Table 2. Overview of the pixel cell parameters used for tests.

| Pitch | Collection n-well size | Spacing |
|----------------------------|------------------------|-------------------|
| $25\times 25\mu\text{m}^2$ | $3\mu\text{m}$ | $3\mu\text{m}$ |
| $28\times 28\mu\text{m}^2$ | $2\mu\text{m}$ | $3\mu\text{m}$ |
| $30\times 30\mu\text{m}^2$ | $3\mu\text{m}$ | $3\mu\text{m}$ |
| $50\times 50\mu\text{m}^2$ | $3\mu\text{m}$ | $18.5\mu\text{m}$ |

signal amplitude and allow to achieve circuit designs optimized for low power and full charge collection efficiency after radiation. To investigate the difference in charge collection before and after irradiation, we measure the output amplitude and signal response time on different pixel designs.

For application in high radiation environments, like the ATLAS experiment, the standard process is not suitable: in the standard process the epitaxial layer at the edges of the pixel is not depleted, resulting in significant charge loss in these regions after irradiation. To obtain fast charge collection by drift we aim at a fully depleted epitaxial layer. To this end, the process was modified with a planar deep n^- -p junction as shown in figure 2. This process modification [6] was developed to extend the depletion region below the deep-p-well. One has to note that the process modification does not require significant layout changes, therefore the same design can be processed in both the standard and modified processes. This process modification has significant influence on the charge collection as will be presented in the following sections. Several samples of the Investigator chip, manufactured using this modified process, have been irradiated with neutrons at the Triga reactor facility, Slovenia. The samples received a fluence of $10^{14}n_{\text{eq}}/\text{cm}^2$ and $10^{15}n_{\text{eq}}/\text{cm}^2$ and the samples were not biased during the irradiations. After irradiation, during and in-between measurements the samples are kept cold at -15°C or less.

3 Setup and analysis

The sensor chips are assembled onto dedicated chip carrier PCBs, which in turn are connected to supply and control boards. The setup allows to select the sub-matrix to be used, provide $V_{dd} = 1.8\text{V}$, substrate voltage (0 to -6V) and route the output signals, one per pixel, of the sub-matrix to external

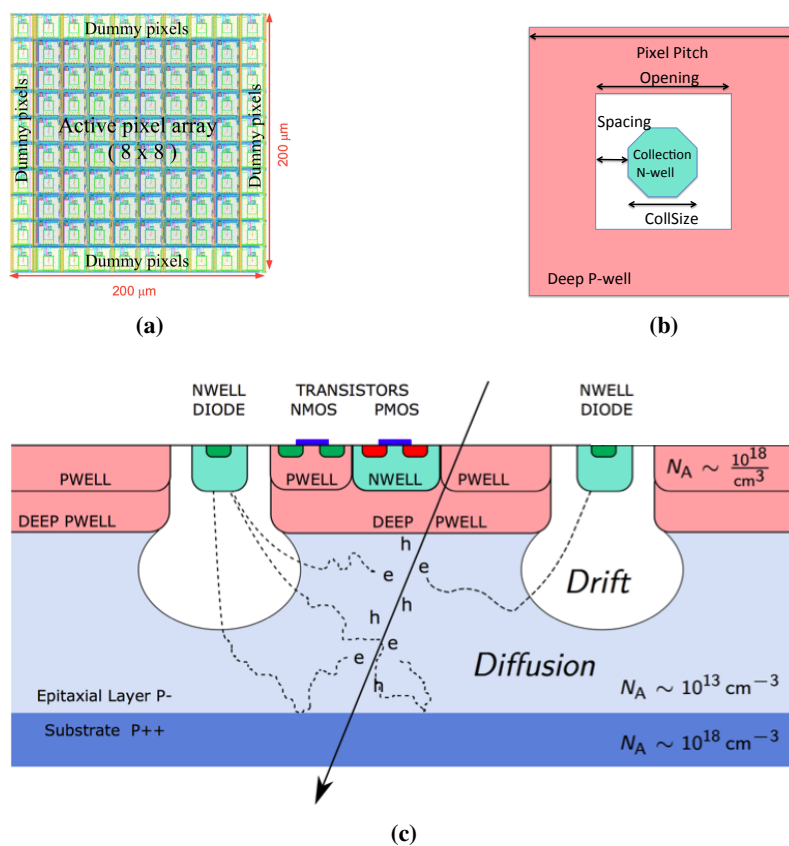


Figure 1. Top view of a sub-matrix (a) and of a pixel (b). (c) Cross-section of the TJ180 standard process for p-type epi silicon and substrate and n-type collection diode.

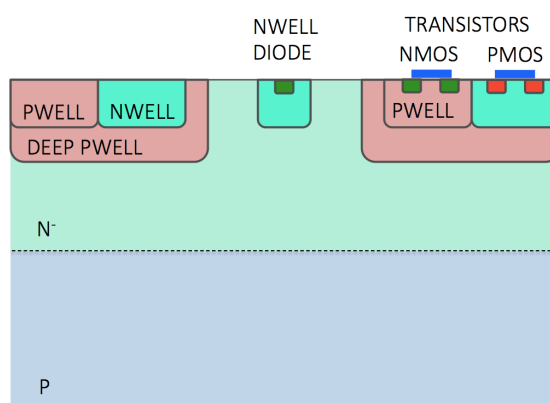


Figure 2. Cross-section of the TJ180 process modification for enhanced depletion.

amplifiers and ADCs. It provides a periodic reset signal ($V_{\text{reset}} = 1\text{V}$) to reset the input transistor, which continuously integrates the input current coming from the collection n-well. We use two different setups to analyse the output pulse: in setup “A” the output of selected channels are amplified using inverting CIVIDEC C1¹ 2GHz broadband amplifiers and then digitised at 5Gps. We use this setup to study in particular the timing properties of the signal at high resolution. In setup “B” no additional amplifier is used and all 64 outputs of a sub-matrix are digitised by ADCs at 65MHz. This setup is typically used to carry out charge-sharing measurements as all 64 channels are recorded simultaneously. In case irradiated samples are used, the test boards are installed in a shielded climate chamber which operates at a temperature of -30°C , to reduce the leakage current. Unirradiated samples are measured at room temperature.

Figure 3a shows the output waveform of a single channel when the pixel is hit by an incident particle shortly after the reset signal (first peak in upper red curve). During the time the reset signal is applied to the front-end, all readout triggers are vetoed, shown as trigger veto (lower black curve). Waveforms are recorded if the amplitude exceeds an amplitude threshold of approximately 300 e^- , to be compared to the expected most probable signal of typically 1700 e^- . Figure 3b shows the analysis of the waveform, which is fitted by an exponential curve shown in red [10]. The figures show the output of Setup “A”, i.e. an oscilloscope recording the output of the external amplifier which is connected to a $50 \times 50\text{ }\mu\text{m}^2$ pixel. The signal amplitude (15.6 mV in this example) and charge collection time (rise-time of 12.58 ns in this example) are extracted from the fits.

4 Charge collection measurements of sensors produced in the standard and modified process

We characterise the signal response in source measurements using ^{55}Fe and ^{90}Sr sources. We use 5.9 keV emitted photons from the ^{55}Fe source to calibrate the signal response of different pixel designs, where the produced photo-electron deposits an ionisation charge of 1640 e- in the sensor. Electrons emitted by ^{90}Sr sources traverse the sensor and generate a signal similar to the response to minimum ionising particles.

4.1 Signal response of sensors with large pixel pitch

Figure 4 shows the comparison of signal response from unirradiated sensors with $50 \times 50\text{ }\mu\text{m}^2$ pixel pitch of the standard (black curves) and modified (red curves) process measured with a substrate voltage $V_{\text{sub}} = -6\text{V}$. Figure 4a shows the amplitude distribution in ^{55}Fe source tests. The change in amplitude gain is due to capacitance increase in the modified process [6]. The sensor input capacitance to the amplifier of this layout in the standard process is estimated at 2.6 fF [9] excluding n-well/p-well junction capacitance. The capacitance depends on the shape of the depletion layer near the collection electrode which is different for the two processes. In the modified process the depleted volume is enlarged under the p-well.

Figure 4a gives the gain calibration constant of $15.9\text{ }\mu\text{V}/\text{e}^-$ and $11.1\text{ }\mu\text{V}/\text{e}^-$ for the standard and modified processes respectively. From the gain reduction from 26 mV to 18 mV, respectively, we estimate the capacitance increase due to process modification to be approximately 30% at a

¹<http://www.cividec.at>.

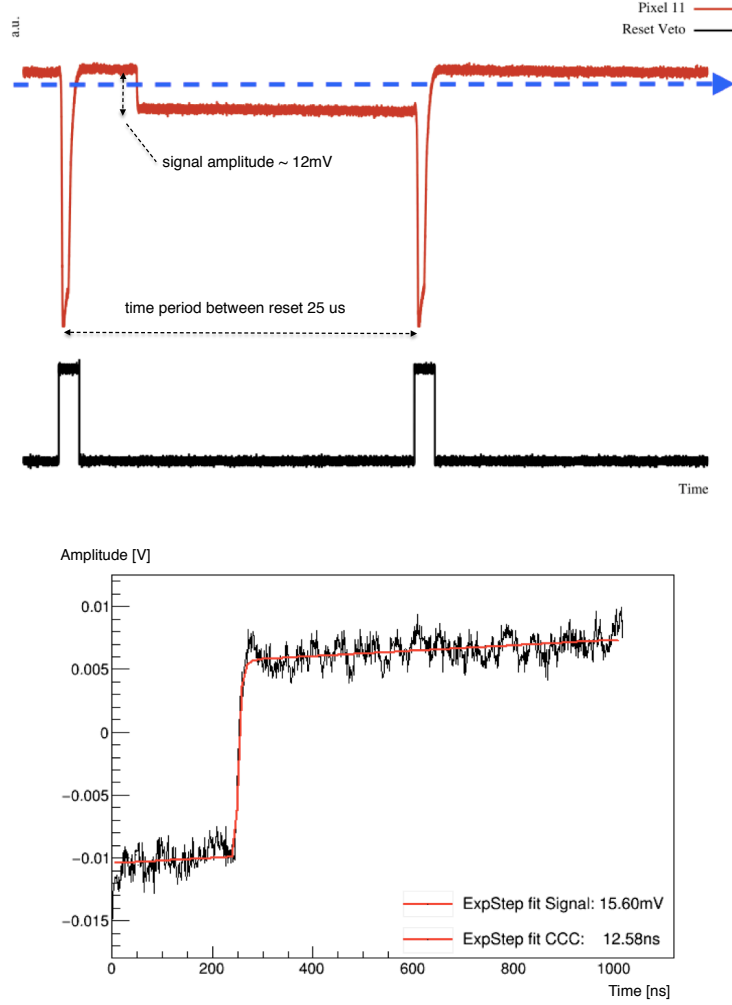


Figure 3. (a) Example output of the Investigator chip (red curve) and trigger veto (black curve). (b) Waveform of setup “A” used for timing measurements. The fit of an exponential step function, shown in red is used to extract the amplitude and signal collection time from a $50 \times 50 \mu\text{m}^2$ pixel.

substrate voltage of -6V. A similar reduction in amplitude is observed in ^{90}Sr sources tests shown in figure 4b. Once the calibration constant is applied to the measured signal amplitudes we observe nearly identical signal distributions as shown in figure 4c. The most probable values for charge collected in standard and modified processes are $1842 e^-$ and $1732 e^-$ respectively. The difference between the curves is within sample to sample variations in our measurements. To compare this to the expected ionisation charge for our sensor, we assume an ionisation charge of $63 e^-$ -h pairs per μm path length [11] and a depletion thickness of $25 \mu\text{m}$, i.e. $1575 e^-$. The slight excess of measured signal over expected signal may be due to contributions from ionisation charge deposited in the transition volume of epitaxial layer to substrate, which we do not include in our calculation. This additional charge from the substrate is expected to contribute additional 10% to the overall measured charge. The signal collection time, given as 10%-90% signal rise time, shows a substantially different behaviour as illustrated in figure 4d. The mean collection times are similar at 15.9 ns and 16.6 ns for standard and modified process, respectively. The width of the distribution,

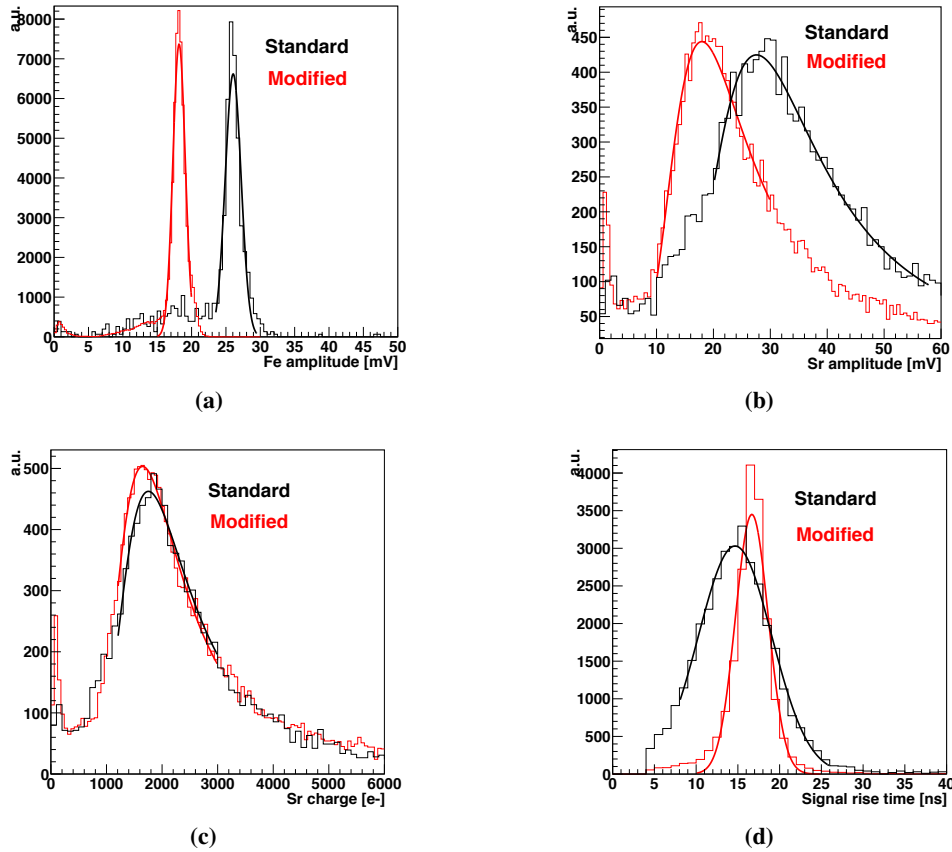


Figure 4. (a) ^{55}Fe source signals of the sub-matrix with a pixel pitch of $50 \times 50 \mu\text{m}^2$. (b) Uncalibrated ^{90}Sr source signals. (c) Calibrated ^{90}Sr source signals. (d) Signal collection times.

however, decreases substantially from 4.6 ns to 1.9 ns in the modified process. The undepleted volumes are significantly reduced as is the contribution from slow diffusion signals. These results indicate a more uniform charge collection mechanism in the modified process as the undepleted volume under the p-well is greatly diminished, hence the contribution of slower diffusion signals is diminished in favour of faster drift signals (cf section 4.3).

4.2 Position resolved charge collection behaviour

We investigate the signal response as function of hit position inside the pixel cell by exposing the unirradiated $50 \times 50 \mu\text{m}^2$ pixel pitch sub-matrix ($3 \mu\text{m}$ electrode diameter, $18.3 \mu\text{m}$ spacing) of the modified process sensor to the monochromatic 15 keV X-ray beam of the DIAMOND X-ray facility.² The facility provides a highly focused X-ray beam of $1.3 \times 2.7 \mu\text{m}^2$ sigma-width, ideally suited to scan across the pixel cell and investigate the uniformity of the sensor's response. Initial 2D scans of the pixel cell, which are read out as described for setup “A”, are used to determine the center of the pixel matrix. Following the initial scan, a high resolution scan was carried out in both X and Y directions. Figure 5 shows the number of hits per 30 seconds on one $50 \mu\text{m}$ pixel as function of

²DIAMOND Light Source, U.K., <http://www.diamond.ac.uk/Home.html>.

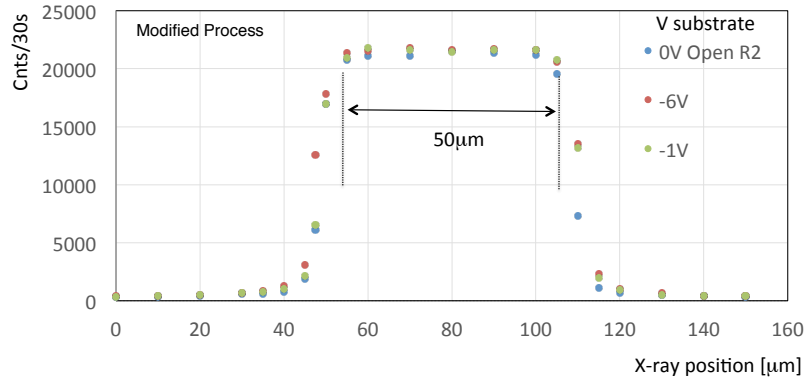


Figure 5. X-ray scan across the pixel cell of a unirradiated $50 \times 50 \mu\text{m}^2$ pixel manufactured in the modified process. The three curves show the number of hits per 30 seconds as function of beam position along a scan line through the pixel center. The three curves are scans at three values of substrate voltage: 0V, -1V, -6V.

beam position for three values of substrate voltage: 0V, -1V, -6V. The scan line was aligned through the center of the pixel. The response is uniform from pixel edge to edge, which is expected from the junction configuration of the modified process (figure 2). Hits are recorded beyond the pixel boundary due to charge sharing between adjacent pixels as a result of diffusion and beam spread. The ionisation charge generated by the 15keV photon is approximately $4140e^-$.

Figure 6 illustrates the charge sharing along the pixel edge of the unirradiated modified process $50 \times 50 \mu\text{m}^2$ pixel. At $\pm 5 \mu\text{m}$ around the edge of the pixel we observe the 15-keV peak together with smaller amplitudes, which stem from signals that are shared between the two adjacent pixels. In $\pm 20 \mu\text{m}$ around the pixel center, shown on the right, we observe primarily signals corresponding to the full 15-keV photo-electron signal. The pixel edges are at beam positions $605 \mu\text{m}$ and $655 \mu\text{m}$. The bottom left plot illustrates this behaviour of amplitude versus beam position. The bottom right plot shows the fitted peak mean amplitude as function of beam position for three different voltages. It should be noted that the amplitude is uniform all across the pixel to better than 3%, even at 0V substrate voltage. The amplitude difference at different substrate voltages is due to the change of capacitance with substrate voltage as the junction enlarges and its capacitance reduces. The small dips of peak amplitude at position $605 \mu\text{m}$ and $655 \mu\text{m}$ are at the pixel edges where the ionisation charge released by the photoelectron is shared between two pixels, i.e. between the pixel connected to the readout and the pixel not connected to the readout. Signals are also recorded when the mean beam position is far outside the pixel acceptance. Those signals stem from beam halo.

4.3 Charge collection and signal rise-times in the standard and modified process

For a better comparison of the charge collection and charge sharing between pixels, in the standard and modified process, we examine the signal response of smaller pitch sensors ($28 \times 28 \mu\text{m}^2$) to ^{55}Fe sources, where the relative fraction of shared hits is increased.

In the standard process the junction is formed at the collection n-well as shown in figure 1. At lower substrate voltages, the extent of the depleted region is limited to the volume around the collection n-well. When the photo-absorption happens in the depleted volume, the signal is collected fast through charge drift and shows the characteristic 5.9 keV peak. The epitaxial volume at larger distances from the collection n-well, especially underneath the p-well, remains undepleted and signal formation is dominated by the diffusion process before the charge carriers reach the

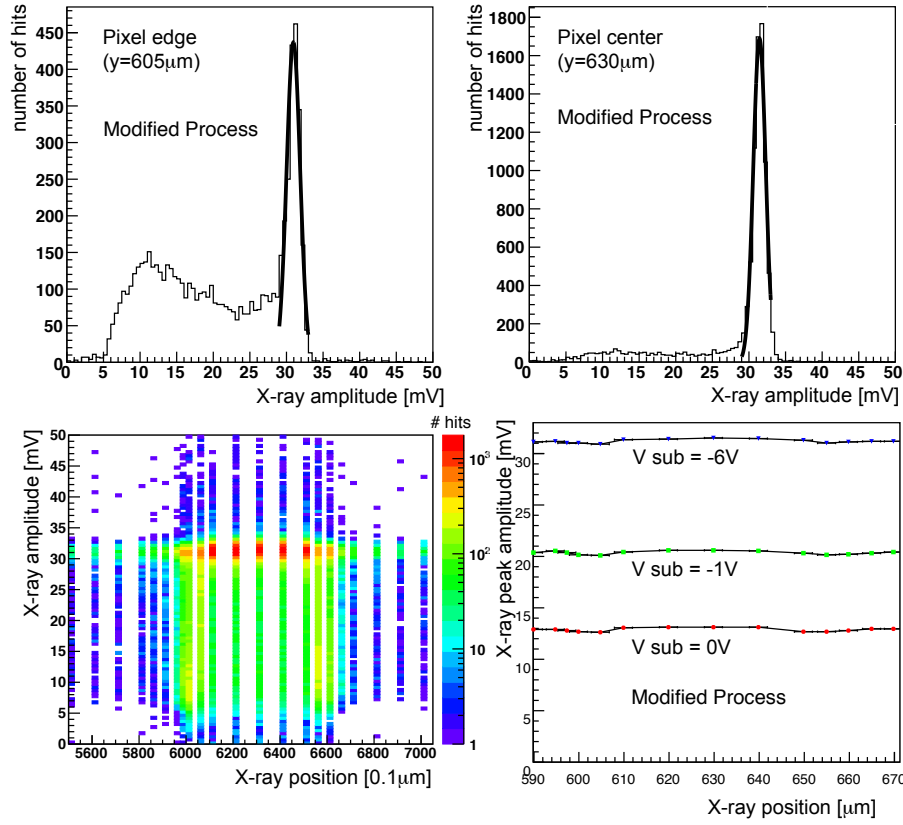


Figure 6. Top row: sensor amplitude distribution recorded at the pixel edge (left) and in pixel center (right). Bottom row: sensor X-ray amplitude distribution versus X-ray position (left) and X-ray signal peak mean as function of beam position at different substrate voltage. Data are taken on an unirradiated $50\times 50\mu\text{m}^2$ pixel manufactured in the modified process.

depleted region. Depending on the position of the photo-absorption, the charge-collection time becomes larger and charge gets shared by several pixels. Figure 7 shows the distributions of single-pixel signal rise times versus signal amplitude in the standard process for three different substrate voltages [8]. At $V_{\text{sub}} = -1\text{V}$ a small ^{55}Fe peak is visible for fast signals at 65mV amplitude. As expected, the signal rise time increases monotonously towards lower signal amplitudes: smaller signals amplitudes with larger rise times are characteristic for charge release in diffusion-dominated regions at increasing distance from the depletion zones. Large signal amplitudes with short rise-times, with the characteristic K_α and K_β peaks of the ^{55}Fe source, stems from ionisation in the depleted zone around the collection n-well. By increasing the substrate voltage we enlarge the depleted volume, which in turn leads to an enhancement of the K_α and K_β peaks and a reduction of signal rise-times even in case of charge sharing. It should also be noted that the signal rise times for the events forming the ^{55}Fe peaks approach the minimum signal rise time of the Investigator chip. Rise-times observed on $28\times 28\mu\text{m}^2$ pixels in this test are consistent with rise-times observed on $50\times 50\mu\text{m}^2$ pixels shown in figure 4d within the uncertainty of differences in measurement setups.³

³Setup specific variations in average rise-times of up to 5ns are possible due to the differences in signal transmission characteristics between setups.

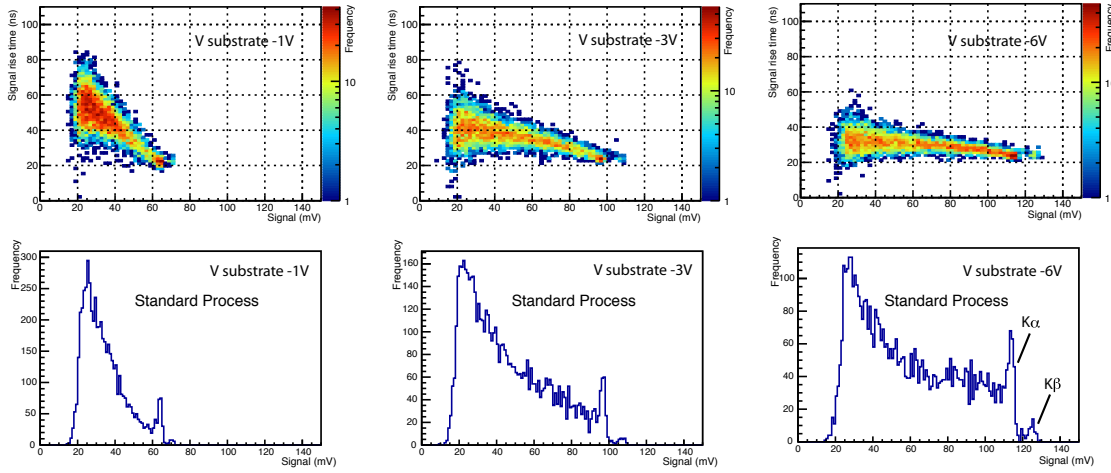


Figure 7. Top row: distribution of signal rise time versus amplitude for an unirradiated $28 \times 28 \mu\text{m}^2$ pixel produced in standard process for three different substrate voltages. Bottom row: amplitude distribution as projections of the two-dimensional histograms.

In the modified process the junction is formed laterally across the epitaxial layer along the interface of the deep planar n^- implant and the p-type epitaxial layer as illustrated in figure 2. This modification significantly enlarges the depleted volume compared to the standard process. Consequently, photo-absorption happens predominantly in depleted volumes and charge sharing is reduced, enhancing the ^{55}Fe peaks (cf. figures 7 and 8). Also charge carriers generated by events at the pixel edges are mostly collected by drift and not by diffusion as in the standard process. This leads to a significant reduction of signal collection times across the whole epitaxial volume. Figure 8 shows the rise-time versus amplitude distributions for a sensor produced in the modified process [8]. At $V_{\text{sub}} = -3\text{V}$ the ^{55}Fe peak is more pronounced than in the standard process which already indicates a significantly larger depleted volume. Also, importantly, the signal rise time is now uniform for all amplitudes. At $V_{\text{sub}} = -6\text{V}$ the ^{55}Fe peak amplitude has increased from 50mV to 87mV due to the related decrease of the junction capacitance. In both signal distributions the K_{α} and K_{β} signals at 5.9keV and 6.3keV are clearly visible and the occurrence of events with lower amplitudes is consistent with geometrical charge sharing along the pixel edges as already described in section 4.2.

From figures 7 and 8 the energy resolution of the pixel sensor is estimated through the FWHM of the K_{α} peak at $54e^-$ for the standard process and $55e^-$ for the modified process. These translate to an energy resolution of 200 eV, which is a remarkably good for such a high granularity pixel sensor. The excellent energy resolution is the result of a sensor design achieving small capacitance through small electrodes combined with improved charge collection of the modified process.

5 Irradiation results

Several sensors have been irradiated with neutrons to $10^{14}n_{\text{eq}}/\text{cm}^2$ and $10^{15}n_{\text{eq}}/\text{cm}^2$ at the Triga reactor facility, Slovenia. Due to the γ -background in the irradiation these samples also received a total-ionising dose (TID) of 100krad and 1Mrad, respectively.

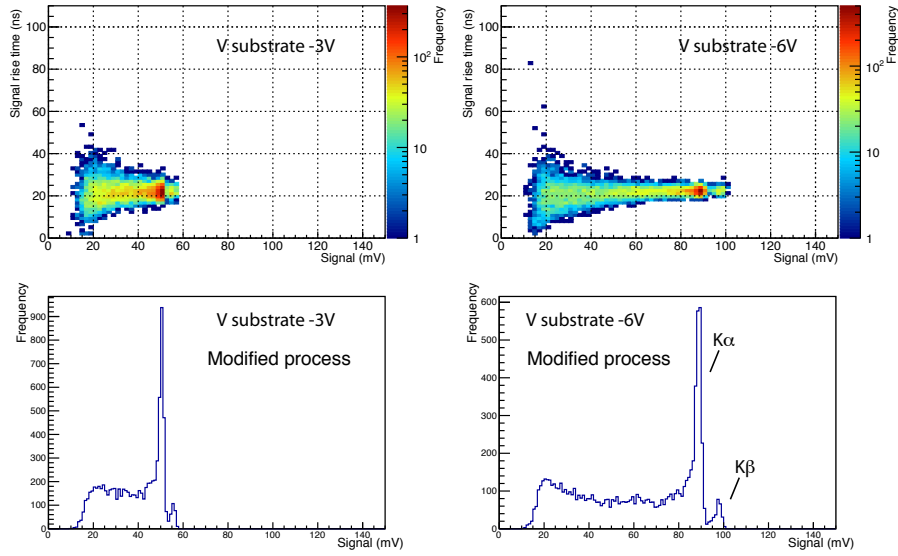


Figure 8. Top row: distribution of signal rise time versus amplitude for the $28 \times 28 \mu\text{m}^2$ pixel produced in modified process for two different substrate voltages. Bottom row: amplitude distribution as projections of the two-dimensional histograms.

5.1 Standard process after irradiation

In the following we compare the signal of unirradiated and irradiated sensors with $50 \times 50 \mu\text{m}^2$ pixel ($3 \mu\text{m}$ electrode diameter, $18.5 \mu\text{m}$ spacing) at relatively low fluence of $10^{14} n_{\text{eq}}/\text{cm}^2$. For this measurement the trigger threshold was kept sufficiently low to include noise triggers in the data sample to illustrate the separation of signal from electronic noise. In the case of ^{90}Sr β source tests, the amplitude distribution follows a convoluted Landau-Gauss distribution. The most probable values (MPV), which are given on the corresponding figures, are extracted from a convoluted Landau-Gauss fit to the data.

Figure 9 shows the signal response of sensors produced in the standard process in ^{90}Sr β source tests (a) and ^{55}Fe γ -source tests (b). A reduction in gain after an irradiation with a dose of $10^{14} n_{\text{eq}}/\text{cm}^2$ irradiation is evident. However the sensor remains fully functional after irradiation. An identical sensor after irradiation to $10^{15} n_{\text{eq}}/\text{cm}^2$ no longer provided signals sufficiently large to allow source measurements and corresponding analysis.

The signal amplitude dependence on substrate voltage for the standard and modified process are illustrated in figure 10 ranging from -1V to -6V . Both samples are irradiated to a fluence of $10^{14} n_{\text{eq}}/\text{cm}^2$. Standard and modified process samples show a similar behaviour: the most-probably value of the Landau-Gauss distribution increases with increasing substrate bias.

5.2 Modified process after irradiation

Due to the different structure and depletion depth between the standard and modified process we expect a significant improvement of radiation hardness for the modified process at higher fluences. Figure 11 compares the results of ^{90}Sr source tests on an unirradiated sample, one sample irradiated to a dose of $10^{14} n_{\text{eq}}/\text{cm}^2$ and one sample irradiated to a dose of $10^{15} n_{\text{eq}}/\text{cm}^2$. All samples are from

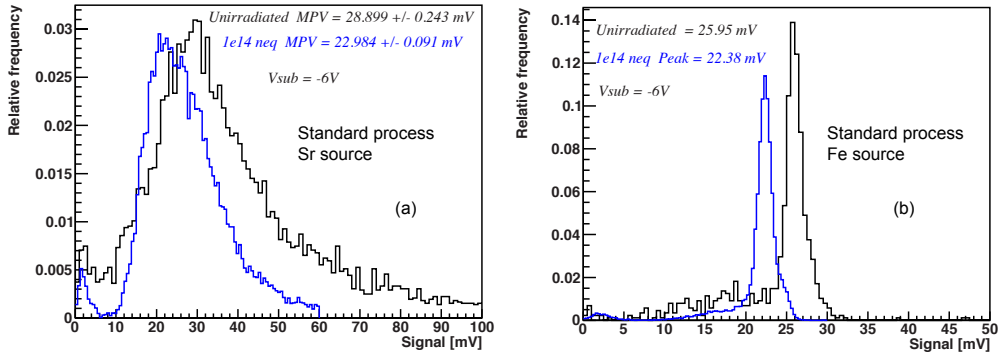


Figure 9. Comparison of sensor response for the $50 \times 50 \mu\text{m}^2$ pixel produced in the standard process before irradiation (black curve) and after a dose $10^{14} n_{\text{eq}}/\text{cm}^2$ (blue curve). Figure (a) shows the amplitude distribution for ^{90}Sr source tests and (b) for ^{55}Fe source tests.

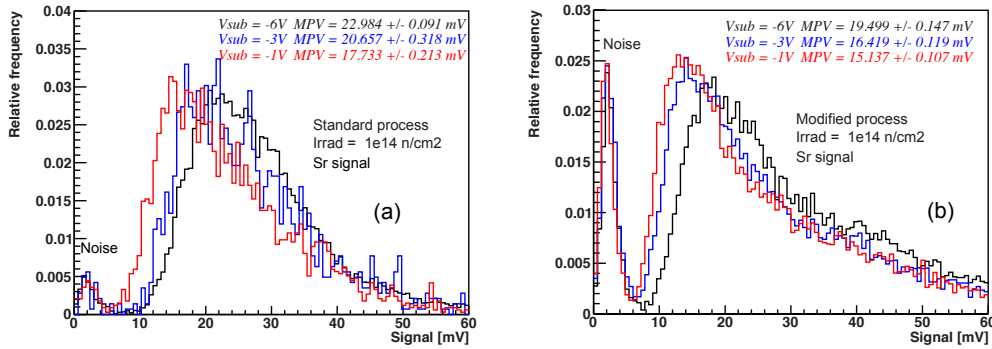


Figure 10. ^{90}Sr source tests amplitudes for the $50 \times 50 \mu\text{m}^2$ pixel produced in the standard process (a) and modified process (b) after $10^{14} n_{\text{eq}}/\text{cm}^2$. The curves show the amplitude response at three different substrate voltages ($-1\text{V}=\text{red}$, $-3\text{V}=\text{blue}$, $-6\text{V}=\text{black}$).

the modified process and were tested at $V_{\text{sub}} = -6\text{V}$. The red curve in figure 11a shows the excellent signal response after a dose of $10^{15} n_{\text{eq}}/\text{cm}^2$, much in contrast to a sensor in the standard process after this irradiation fluence. Figure 11b shows the signal collection times. The sensor maintains the fast signal response even after a dose of $10^{15} n_{\text{eq}}/\text{cm}^2$. A small increase of signal collection time from 16.7 ns to 19 ns is observed with a slight increase of spread from $\sigma = 1.96 \text{ ns}$ to $\sigma = 2.78 \text{ ns}$. The time spread after $10^{15} n_{\text{eq}}/\text{cm}^2$ is still significantly less than for the unirradiated sensor of the standard process which gave 4.6 ns as shown in figure 4d. Rise-time differences between figure 11b and figure 8 are likely due to test setup differences, as the two measurements use different external amplification and digitisation chains after the Investigator sample.

To investigate the slight reduction of signal amplitude at $10^{15} n_{\text{eq}}/\text{cm}^2$, we carried out a calibration with a ^{55}Fe source. Figure 12 shows the amplitude distribution of the 5.9keV photo-electron for the unirradiated sensor, a sensor irradiated to a dose of $10^{14} n_{\text{eq}}/\text{cm}^2$ and one sample irradiated to a dose of $10^{15} n_{\text{eq}}/\text{cm}^2$. We observe a slight reduction in amplifier gain with increasing irradiation fluence, which matches approximately the amplitude reduction observed in the ^{90}Sr source tests.

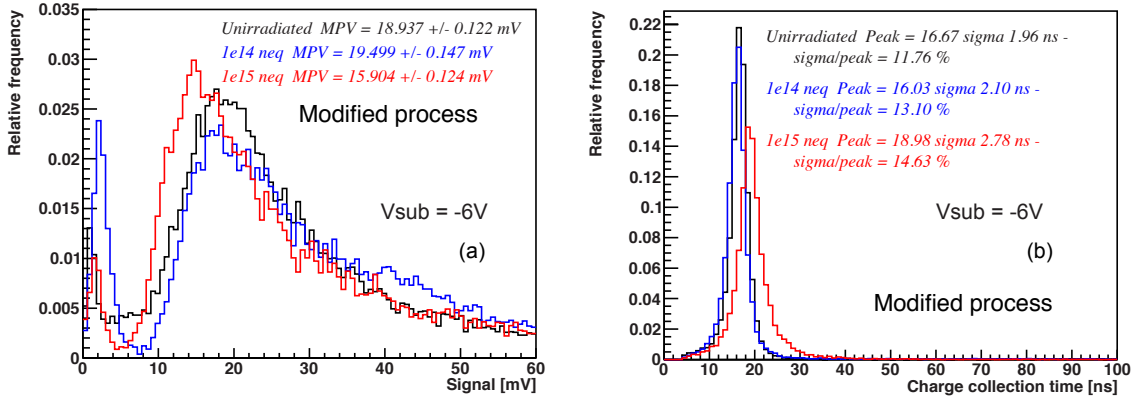


Figure 11. Signal response of $50 \times 50 \mu m^2$ pixel pitch produced in the modified process before irradiation (black curves), after $10^{14} n_{eq}/cm^2$ (blue curve) and after $10^{15} n_{eq}/cm^2$ (red curve). Figure (a) shows the amplitude distribution for ^{90}Sr source tests and plot (b) the signal collection time.

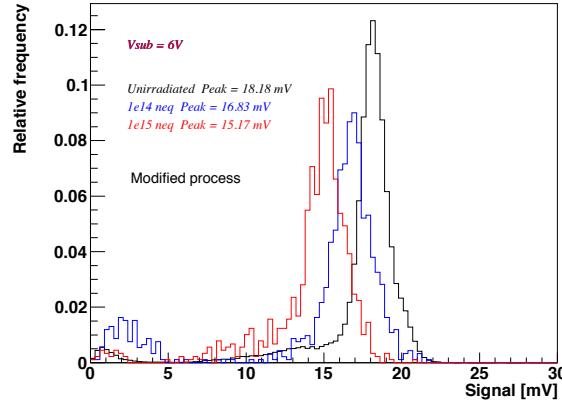


Figure 12. ^{55}Fe signal response of $50 \times 50 \mu m^2$ pixel pitch produced in the modified process before irradiation (black curves), after $10^{14} n_{eq}/cm^2$ (blue curve) and after $10^{15} n_{eq}/cm^2$ (red curve).

Using the ^{55}Fe source calibration we convert the sensor amplitude to deposited charge and generate the charge distributions for irradiated samples. Figures 13a and 13b show for ^{90}Sr source measurements the charge distribution and charge distributions as a function of collection time of the unirradiated sensor. Figure 13c and figure 13d show the corresponding distributions for the sensor irradiated to a dose of $10^{15} n_{eq}/cm^2$. After calibration the charge distributions for unirradiated and irradiated sensors yield comparable most probable charge values of $1732 e^-$ and $1740 e^-$, respectively. The spread of the collection times increase slightly for the irradiated sensors. The recorded charge distribution's most probable value agrees well with a fully depleted sensor. Further measurements are currently in progress to investigate the sensor performance up to $10^{16} n_{eq}/cm^2$.

6 Beam Test results

To measure the detection efficiency we installed the CMOS sensors together with a silicon pixel reference telescope in the CERN SPS test beam. The beam delivers 180 GeV/c pions, which are

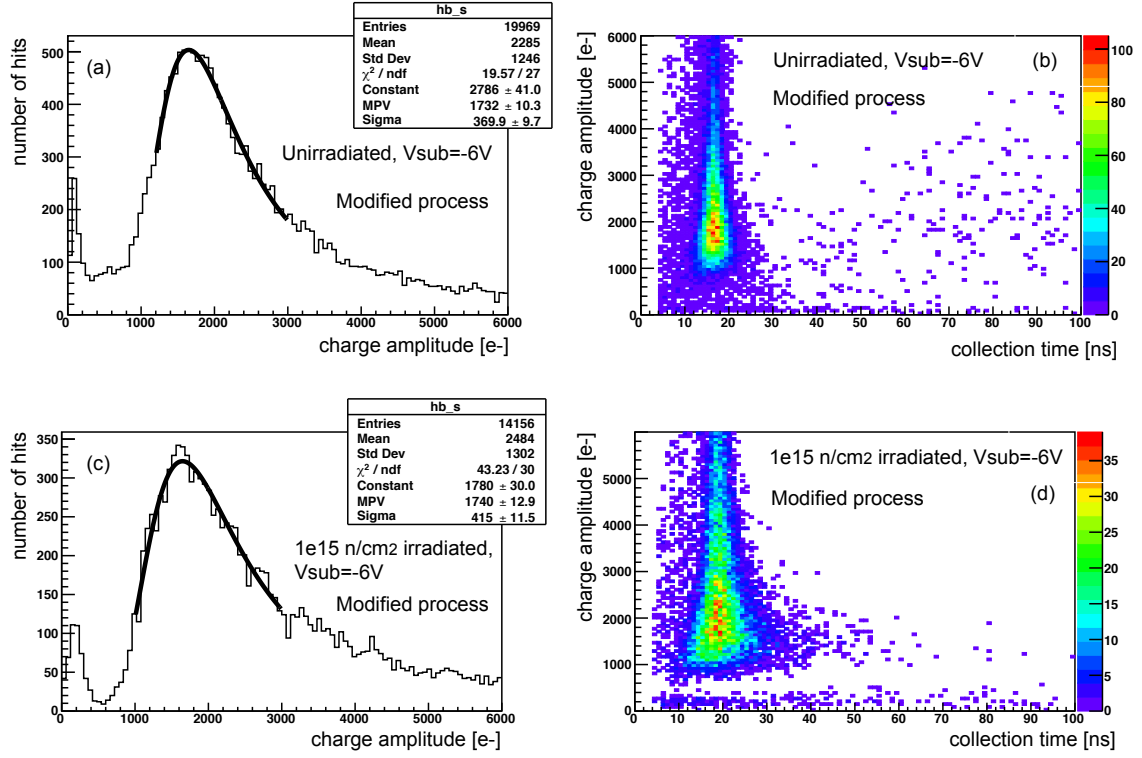


Figure 13. Signal response of $50 \times 50 \mu\text{m}^2$ pixel pitch produced in the modified process before irradiation (plot a and b) and after $10^{15} \text{ n}_{\text{eq}}/\text{cm}^2$ (plot c and d). Figure (a) and (c) shows the charge amplitude distribution for ^{90}Sr source tests and plot (b) and (d) show the charge versus signal collection time.

recorded and reconstructed in the reference telescope [12, 13] and extrapolated to the device under test (DUT) with a spatial resolution of $9 \mu\text{m}$.

The DUT, which are sensors produced in the modified process, is placed in the middle of the telescope with three silicon pixel reference planes upstream and three silicon pixel reference planes down-stream. Each reference plane consists of one FE-I4 chip [14] bump-bonded to a planar n-in-n silicon pixel detector. The pixel pitch on the FE-I4 is $50 \times 250 \mu\text{m}^2$. The telescope has every other plane rotated by 90° around the beamline so that the resolution in the X and Y planes are similar. Furthermore every other reference plane is tilted by 15° around the pixel long-side axis to improve the spatial resolution in the pixel short-side direction through charge sharing and hit position interpolation.

Hits are required on two layers of the telescope in a region of interest to trigger the readout of telescope and DUT. The resulting data is reconstructed with the “Judith” reconstruction software [15]. Judith aligns the telescope by iteratively minimizing the track to hit residuals for tracks reconstructed with hits on “N-1” of the planes.

6.1 Measurement of cluster size

From the sensor matrix a 2×2 -pixel subset in the center of the matrix under test are readout using 4 broadband amplifiers as described for Setup “A”. During the beam test we used only pixel sensors manufactured in the modified process. Hits on the DUT are correlated to reconstructed tracks. The

collected charge and the noise during the beam tests have been measured with a substrate voltage of -6V. Each run is individually aligned to correct for movements between reference planes and/or DUT. The full waveform is readout from the DUT and used to extract the charge collection time, the hit detection time (t_0), and the signal amplitude. Two selection criteria are considered to remove noise hits. The first criteria selects on the hit detection time in the range of ± 60 ns around the trigger time. The second criteria cuts on the minimal amplitude of 4mV, which translate to an effective charge threshold of $50e^-$ to $100e^-$ on the $25 \times 25 \mu\text{m}^2$ and $30 \times 30 \mu\text{m}^2$ pixel sensors that have a small spacing of $3 \mu\text{m}$ and show a large signal gain. The $50 \times 50 \mu\text{m}^2$ pixel sensors use a large spacing ($18.5 \mu\text{m}$), they exhibit a small signal gain, and consequently the 4mV threshold translate to a charge of approximately $600e^-$. We also require that the charge collection time is less than 250 ns.

The extrapolated hit position is then used to study the collected charge and cluster size as function of hit position in the pixel as shown in figure 14. Figure 14a shows cluster charge of the $50 \times 50 \mu\text{m}^2$ pixel (spacing $18.5 \mu\text{m}$) sensor as function of hit position for an unirradiated sensor. The cluster charge is calculated as the sum of amplitudes for all pixels above threshold. Figure 14b gives the cluster size as number of pixels above threshold. The charge sharing along the pixel edge is visible through an increased cluster size at the X- and Y-axis. The amplitude distribution is shown in 14c together with the electronic noise. The Landau distributed signal is well separated from the Gaussian noise with a Signal-to-Noise Ratio (SNR) of $\approx 13:1$. The SNR of smaller pixel pitch sensors, which also have smaller spacing, is larger with 39:1 for the $25 \times 25 \mu\text{m}^2$ pixel (spacing $3 \mu\text{m}$) sensors after $10^{15} n_{\text{eq}}/\text{cm}^2$ and 33:1 for the $30 \times 30 \mu\text{m}^2$ pixel (spacing $3 \mu\text{m}$) sensors after a dose of $10^{15} n_{\text{eq}}/\text{cm}^2$. Figure 15 shows the cluster size for the unirradiated $50 \times 50 \mu\text{m}^2$ pixel sensor (blue), for the $25 \times 25 \mu\text{m}^2$ pixel sensor after a dose of $10^{15} n_{\text{eq}}/\text{cm}^2$ (red) and for the $30 \times 30 \mu\text{m}^2$ pixel sensors after a dose of $10^{15} n_{\text{eq}}/\text{cm}^2$ (green). While single-pixel clusters dominate the response of the $50 \times 50 \mu\text{m}^2$ pixel sensors (mean 1.06), we find approximately 30% of double-pixel clusters on the $25 \times 25 \mu\text{m}^2$ or $30 \times 30 \mu\text{m}^2$ pixel sensors (mean 1.35 and 1.37 respectively). In addition to the pixel pitch, the cluster width is influenced by the spacing between n-well and p-well, which is $3 \mu\text{m}$ for the $25 \times 25 \mu\text{m}^2$ and $30 \times 30 \mu\text{m}^2$ pixels, while it is $18.5 \mu\text{m}$ for $50 \times 50 \mu\text{m}^2$ pixels.

6.2 Measurement of sensor efficiency

With an acceptance of only four pixels ($50 \times 50 \mu\text{m}^2$ to $100 \times 100 \mu\text{m}^2$ for $25 \mu\text{m}$ and $50 \mu\text{m}$ pitches respectively) the detection efficiency calculation is influenced by edge effects of the acceptance area and the limited position resolution of the telescope of $\approx 9 \mu\text{m}$. To correct for this edge effects we simulate what efficiency would be obtained in this setup if the sensor would be 100 % efficient. This is shown in figure 16. Figure 16a shows the probability that a track actually crossed the sensor in the 4-pixels area with $50 \times 50 \mu\text{m}^2$ pixel pitch if the hit is predicted on the sensor surface with an accuracy of $\approx 9 \mu\text{m}$, which is the measured telescope resolution. Folding this probability with the measured efficiency as function of track impact position allows for the correction of acceptance edge effects in our efficiency measurements. From this calculation we also estimate the systematic uncertainty of the efficiency calculation by varying the telescope resolution up and down by $\pm 1 \mu\text{m}$. The resulting uncertainty is shown in figure 16b. The result shows that the error in the efficiency measurement, due to telescope resolution and alignment accuracy, is minimised if the measurement area is restricted to the area between the four pixel centres. The area defined through the four pixel

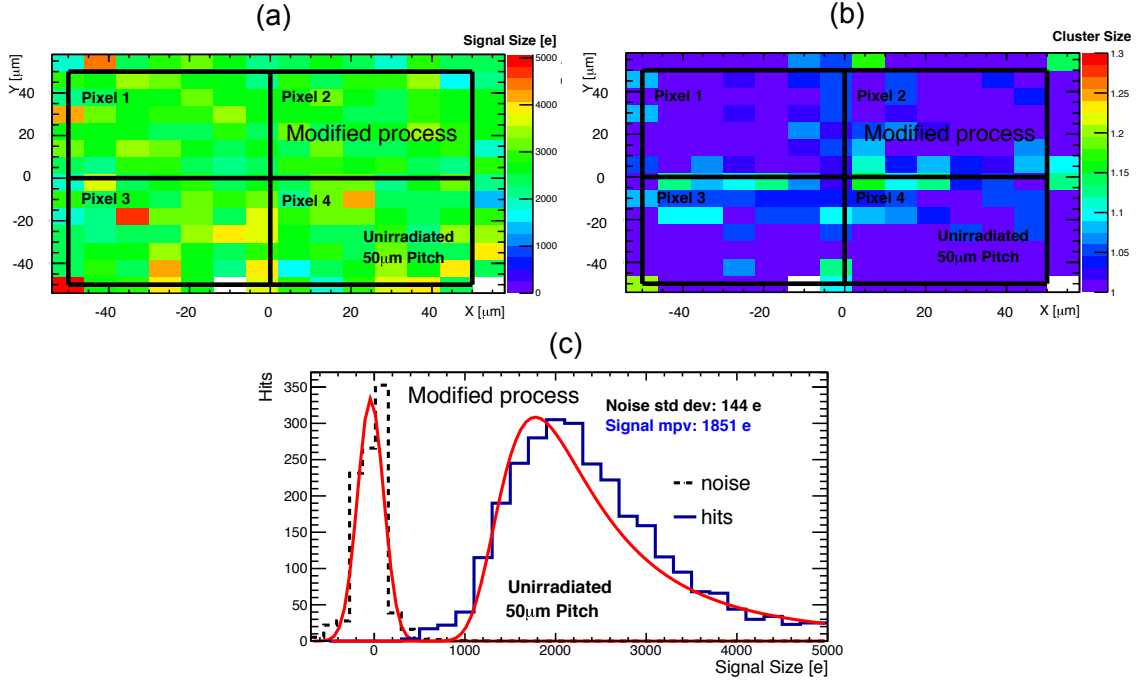


Figure 14. (a) Charge as function of hit position for the unirradiated modified process $50 \times 50 \mu\text{m}^2$ pixel sensor with $3 \mu\text{m}$ electrode and $18.5 \mu\text{m}$ spacing. (b) Cluster size as function of hit position. (c) Signal and noise distributions as measured in the test beam on this sensor.

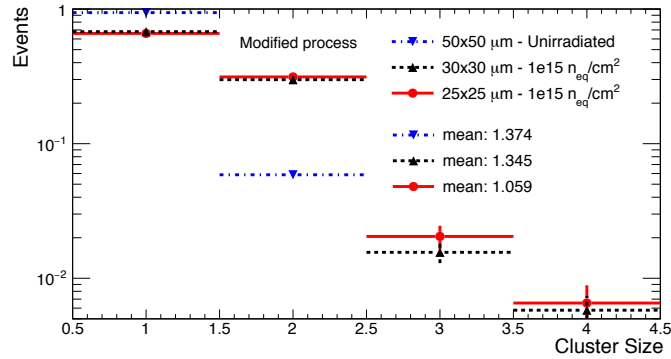


Figure 15. Cluster size for the unirradiated modified process $50 \times 50 \mu\text{m}^2$ pixel sensor (blue), for the $25 \times 25 \mu\text{m}^2$ pixel sensor after $10^{15} n_{eq}/\text{cm}^2$ (red) and for a $30 \times 30 \mu\text{m}^2$ pixel pitch sensors after $10^{15} n_{eq}/\text{cm}^2$ (green).

center locations as illustrated by the green area of figure 16c is also a representative area for the full pixel because it includes collection electrodes (center) as well as pixel boundaries and corners.

6.3 Efficiency before irradiation

To investigate the efficiency uniformity across the sensor, we calculate it as function of extrapolated hit position in X and Y coordinates. The efficiency is the ratio of the number of events with telescope tracks and a corresponding sensor hit to the number of all events with a telescope track. The hit efficiency is shown versus the x and y-position of the track relative to the aligned sensor position

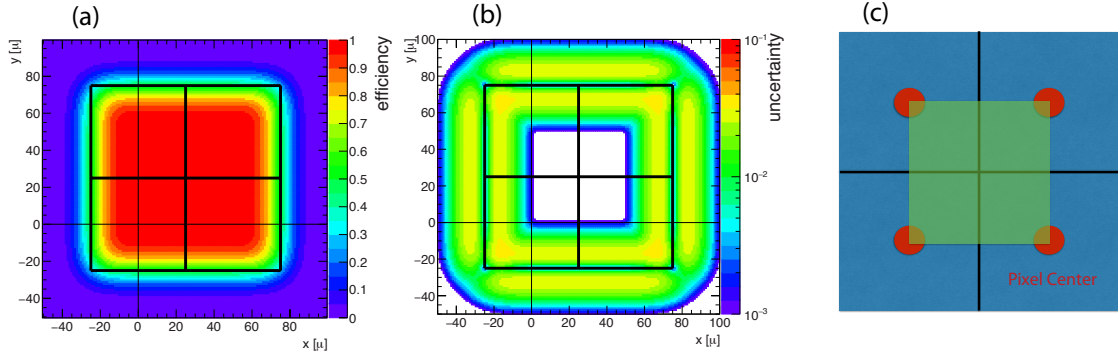


Figure 16. (a) Calculated detector efficiency as function of the hit position. (b) Calculated efficiency uncertainty using the telescope resolution of $\approx 9\mu\text{m}$. (c) Selection area for efficiency calculation.

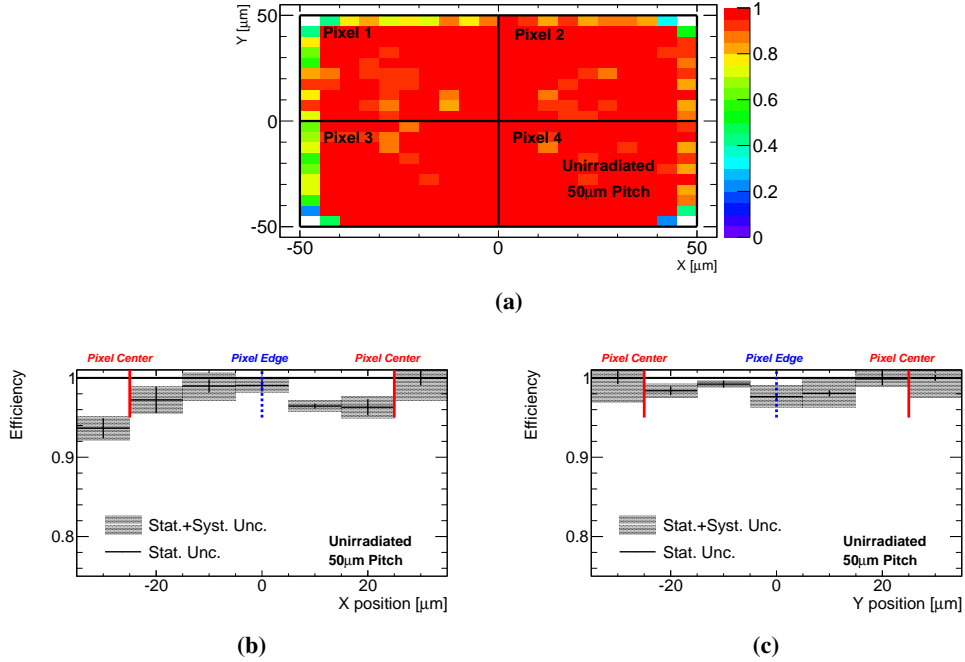


Figure 17. Detector efficiency as function of the hit position for an unirradiated modified process $50 \times 50 \mu\text{m}^2$ pixel sensor with $3\mu\text{m}$ electrode and $18.5\mu\text{m}$ spacing (a). Efficiency projection between the pixel centers in X and Y direction as shown in graph (b) and (c).

in figure 17. The figure shows the acceptance corrected efficiency as measured on an unirradiated modified process $50 \times 50 \mu\text{m}^2$ pixel sensor with $3\mu\text{m}$ electrode and $18.5\mu\text{m}$ spacing. The efficiency is shown across the 4-pixels area (a) and the projection onto the X-axis (b) and Y-axis (c). The efficiency is uniform across the pixel and is measured to be $98.5\% \pm 0.5\%$ (stat) $\pm 0.5\%$ (syst) overall. The overall efficiency is limited to slightly below 100% because of the rather high signal threshold ($\approx 600\text{ e}^-$ on this sensor), which was required to cope with higher noise in the test beam setup due to common mode noise during the measurements of this sensor matrix.

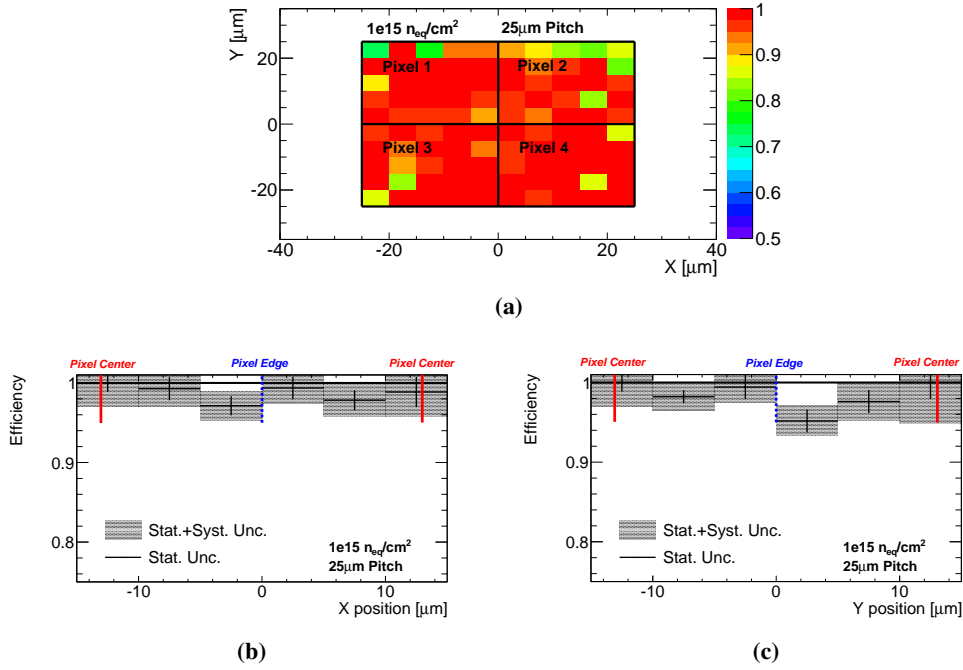


Figure 18. Detector efficiency as function of the hit position for an $10^{15} n_{eq}/\text{cm}^2$ irradiated modified process $25 \times 25 \mu\text{m}^2$ pixel sensor with $3 \mu\text{m}$ electrode and $3 \mu\text{m}$ spacing (a). Efficiency projection between the pixel centers in X and Y direction as shown in graph (b) and (c).

6.4 Efficiency after irradiation

In the following we investigate the efficiency of sensors of the modified process, which were irradiated to a dose of $10^{15} n_{eq}/\text{cm}^2$. Figure 18 shows the efficiency for a sensor with a pixel pitch of $25 \mu\text{m}$ and small spacing ($3 \mu\text{m}$) around the collection n-well. For this sensor we observe full efficiency uniformly across the detector. The overall efficiency integrated over the pixel cell area was found to be $98.5\% \pm 1.5\%$ (stat) $\pm 1.2\%$ (syst).

Figure 19 shows the efficiency for a sensor irradiated to $10^{15} n_{eq}/\text{cm}^2$ with a pixel pitch of $30 \mu\text{m}$ and small spacing ($3 \mu\text{m}$) around the collection n-well. For this sensor the measured efficiency is uniform across the pixel cell at $97.4\% \pm 1.5\%$ (stat) $\pm 0.6\%$ (syst). These results demonstrate the substantial improvement of radiation hardness achieved through the process modification with a planar n-layer.

7 Summary

The ATLAS collaboration currently investigates radiation hard CMOS sensors for possible application in the upgrade of its pixel tracker upgrade for the High-Luminosity LHC. Using an existing monolithic pixel prototype sensor, the “Investigator” chip, developed by the ALICE Collaboration, we have investigated and compared signal collection characteristics, detection efficiency, and tolerance to non-ionizing radiation of this sensor produced both in the standard TowerJazz 180 nm CMOS imager process and in a version of this process modified to create a planar junction deep in the epitaxial layer and obtain full depletion of the epitaxial layer.

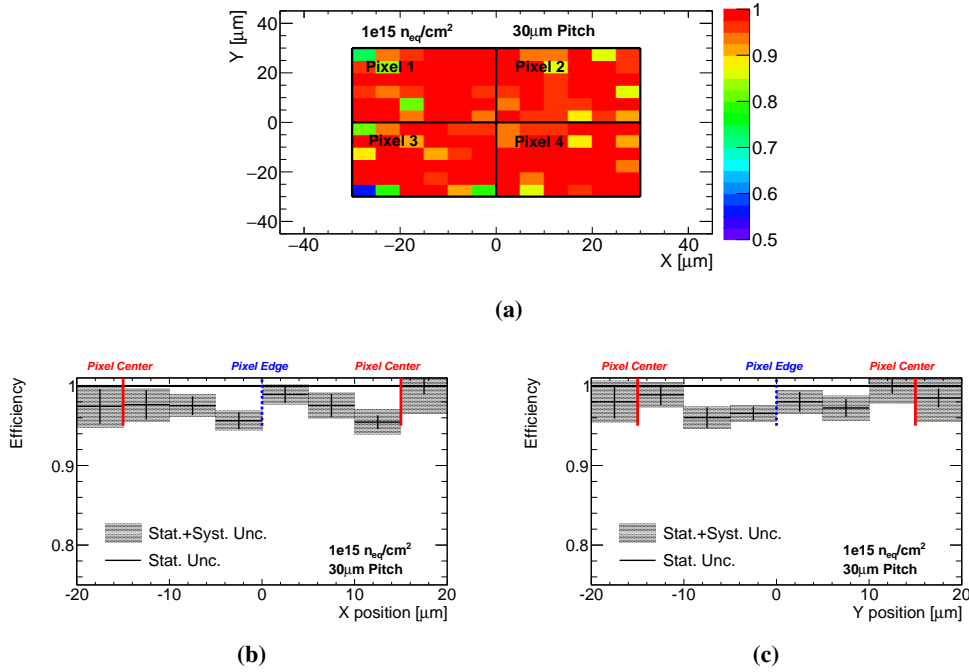


Figure 19. Detector efficiency as function of the hit position for an $10^{15} n_{eq}/cm^2$ irradiated modified process $30 \times 30 \mu m^2$ pixel sensor with $3 \mu m$ electrode and $3 \mu m$ spacing (a). Efficiency projection between the pixel centers in X and Y direction as shown in graph (b) and (c).

The standard process yields good efficiency at low radiation levels for small collection electrode sizes, but suffers from non-uniformity in charge collection and efficiency drop on the edges at higher irradiation doses. Measurements indicate full depletion of the sensors produced in the novel modified process. This combined with pixels cells with small, low capacitance collection electrodes enables low power pixel design with high radiation tolerance. The new sensors show significantly improved signal behaviour with faster, more uniform signals and no charge loss even at $10^{15} n_{eq}/cm^2$, the expected NIEL radiation fluence for the ATLAS ITk pixel outer layers.

Beam tests using the 180 GeV/c pion beam of the CERN SPS accelerator yield a detection efficiency of $98.5\% \pm 0.5\%$ (stat) $\pm 0.5\%$ (syst) before irradiation for the $50 \times 50 \mu m^2$ pixel with n-well/p-well spacing of $18.5 \mu m$ between collection n-well and surrounding deep p-well. The efficiency of an $10^{15} n_{eq}/cm^2$ irradiated sample with $30 \times 30 \mu m^2$ with $3 \mu m$ electrode and $3 \mu m$ spacing showed an overall efficiency of $97.4\% \pm 1.5\%$ (stat) $\pm 0.6\%$ (syst), uniform across the pixel within the resolution of our reference telescope, indicating no significant loss of efficiency due to irradiation despite the small collection electrode of only $3 \mu m$ electrode diameter on a $30 \mu m$ pixel pitch.

Further studies are progressing towards irradiation results up to a dose of $10^{16} n_{eq}/cm^2$. The encouraging results obtained on the Investigator chip allow us to prepare designs for more complex, full reticle-size depleted monolithic CMOS pixel sensors, meeting the challenging requirements of future tracking detectors at HL-LHC.

Acknowledgments

The authors are very grateful to Dr. Igor Mandic and Dr. Vladimir Cindro of the Institute Jozef Stefan, Ljubljana, Slovenia for their support during neutron irradiation campaign. The irradiation campaign has been supported by the H2020 project AIDA-2020, GA no. 654168. The authors would like to thank personnel of the B16 beam line of Diamond Light Source, Andy Malandine and Kawal Sawhney, as well as Andrew Blue, University of Glasgow, and Luise Poley, Deutsches Elektronen-Synchrotron Germany, for providing support during the X-ray measurements carried out under the STFC grant ST/K001205/1. The authors would further like to thank Dr. Erich Griesmayer of CIVIDEC GmbH, Vienna, for his assistance with broadband amplifiers.

References

- [1] ATLAS collaboration, *The ATLAS experiment at the CERN Large Hadron Collider*, [2008 JINST 3 S08003](#).
- [2] G. Aglieri et al., *Monolithic active pixel sensor development for the upgrade of the ALICE inner tracking system*, [2013 JINST 8 C12041](#).
- [3] S. Senyukov et al., *Charged particle detection performances of CMOS pixel sensors produced in a 0.18 μm process with a high resistivity epitaxial layer*, *Nucl. Instrum. Meth. A* **730** (2013) 115 [[arXiv:1301.0515](#)].
- [4] ATLAS collaboration, *ATLAS phase-II upgrade scoping document*, [CERN-LHCC-2015-020](#), CERN, Geneva Switzerland, (2015).
- [5] G. Aad et al., *ATLAS pixel detector electronics and sensors*, [2008 JINST 3 P07007](#).
- [6] W. Snoeys et al., *A process modification for CMOS Monolithic Active Pixel Sensors for enhanced depletion, timing performance and radiation tolerance*, submitted for publication in *Nucl. Instrum. Meth. A*.
- [7] J. Willem van Hoorne, *Study and development of a novel silicon pixel detector for the upgrade of the ALICE Inner Tracking system*, Ph.D. thesis, [CERN-THESIS-2015-255](#), TU Vienna, Vienna Austria, (2015), pg. 61.
- [8] J. Willem van Hoorne et al., *The investigator — an efficient tool to optimize design parameters of a CMOS pixel sensor*, presentation at the *IEEE NSS/MIC 2016 conference*, Strasbourg France, November 2016.
- [9] C. Gao et al., *A novel source-drain follower for monolithic active pixel sensors*, in *Proceedings of the 10th International “Hiroshima” Symposium on the Development and Application of Semiconductor Tracking Detectors*, Elsevier, The Netherlands, (2016) [*Nucl. Instrum. Meth. A* **831** (2016) 147].
- [10] C. Riegel et al., *Radiation hardness and timing studies of a monolithic TowerJazz pixel design for the new ATLAS Inner Tracker*, in *Proceedings of the 18th International Workshop on Radiation Imaging Detectors*, Barcelona Spain, (2016) [[2017 JINST 12 C01015](#)].
- [11] S. Meroli, D. Passeri and L. Servoli, *Energy loss measurement for charged particles in very thin silicon layers*, [2011 JINST 6 P06013](#).
- [12] ATLAS SBM Beam Test Telescope webpage, <http://ade-pixel-group.web.cern.ch/ade-pixel-group/TestBeam/>.

- [13] *ATLAS-SBM1-AIDA Telescope user guide*,
<https://twiki.cern.ch/twiki/bin/view/Main/ATLASSBMAIDATELESCOPEUserGuide>.
- [14] ATLAS collaboration, *ATLAS insertable B-layer technical design report*, [CERN-LHCC-2010-013](#), CERN, Geneva Switzerland, (2010) [ATLAS-TDR-19].
- [15] G. McGoldrick et al., *Synchronized analysis of testbeam data with the Judith software*, *Proceedings of the 9th International “Hiroshima” Symposium on the Development and Application of Semiconductor Tracking Detectors*, Elsevier, The Netherlands, (2014) [*Nucl. Instrum. Meth. A* **765** (2014) 140].